JACS
JOURNAL OF THE AMERICAN CHEMICAL SOCIETY
pubs.acs.org/JACS
Article

# *In Situ* Active Site for CO Activation in Fe-Catalyzed Fischer–Tropsch Synthesis from Machine Learning

Qian-Yu Liu, Cheng Shang,* and Zhi-Pan Liu*

Cite This: *J. Am. Chem. Soc.* 2021, 143, 11109–11120
Read Online



**ABSTRACT:** *In situ*-formed iron carbides ($FeC_x$) are the key components responsible for Fischer–Tropsch synthesis (FTS, CO + $H_2$ → long-chain hydrocarbons) on Fe-based catalysts in industry. The true active site is, however, highly controversial despite more than a century of study, which is largely due to the combined complexity in both $FeC_x$ structures and mechanism of CO hydrogenation. Herein powered by machine learning simulation, millions of structure candidates for $FeC_x$ bulk and surfaces are explored under FTS conditions, which leads to resolving the active site for CO activation. This is achieved without *a priori* input from experiment by first constructing the thermodynamics convex hull of bulk phases, followed by identifying the low surface energy surfaces and evaluating the adsorption ability of CO and H, and finally determining the lowest energy reaction pathway of CO activation. Rich information on $FeC_x$ structures and CO hydrogenation pathways is gleaned: (i) $Fe_5C_2$, $Fe_7C_3$, and $Fe_2C$ are the three stable bulk phases under FTS in producing olefins, where $Fe_7C_3$ and $Fe_2C$ have multiple energetically nearly degenerate bulk crystal phases; (ii) only three low surface energy surfaces of these bulk phases, namely, $\chi$-$Fe_5C_2$(510), $\chi$-$Fe_5C_2$(111), and $\eta$-$Fe_2C$(111), expose the Fe sites that can adsorb H atoms exothermically, where the surface Fe:C ratio is 2, 1.75, and 2, respectively; (iii) CO activation via direct dissociation can occur at the surface C vacancies (e.g., with a barrier of 1.1 eV) that are created dynamically via hydrogenation. These atomic-level understandings facilitate the building of the structure–activity correlation and designing better FT catalysts.

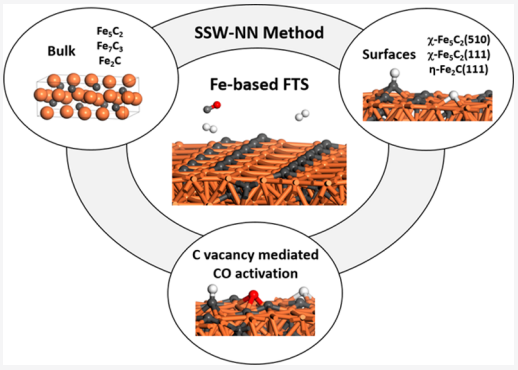


## 1. INTRODUCTION

Fischer–Tropsch synthesis (FTS) is a key technology to convert syngas into liquid fuels that can be catalyzed by several group-VIII elements (Fe, Co, and Ru). Unlike the Co and Ru catalysts, the iron-based catalyst tends to form multiple iron carbide ($FeC_x$) phases at FTS conditions (423–623 K, 2–3 MPa, and $H_2$/CO = 2). These $FeC_x$ phases are metastable and undergo reverse phase transition to iron (oxide) when leaving the FTS condition; that is, the *ex situ* analysis without CO/$H_2$ gases cannot observe the correct carbide active phases. It is thus extremely challenging to characterize and identify the active site from these *in situ*-formed carbide phases despite more than 100 years' research.[1−8] Intriguingly, virtually all iron carbides detected under FTS conditions, typically by X-ray diffraction (XRD) and Mössbauer spectroscopies, were suggested to be responsible for the catalytic activity to produce hydrocarbons.[9−14] New *in situ* techniques are called for to resolve the active site and clarify the CO activation mechanism.

To date, a variety of $FeC_x$ phases, including $\theta$-$Fe_3C$, $\chi$-$Fe_5C_2$, $Fe_7C_3$, $\varepsilon'$-$Fe_{2.2}C$, and $\varepsilon$-$Fe_2C$, were identified in FT experiments, and thus the operating FT catalyst should be a mixture of different $FeC_x$ phases.[9,15−18] Based on the experimental crystal data, recent density functional theory (DFT) calculations[16] confirm the phase complexity of $FeC_x$ under reaction conditions, where the formation energy of various $FeC_x$ phases is close, i.e., within ∼0.1 eV per C atom.

The active $FeC_x$ phase is however highly debated since all the observed $FeC_x$ phases appear to be active for FTS, but with different selectivity. In general, the high Fe:C ratio phase $Fe_3C$ is utilized in the high-temperature FTS (>600 K) and prefers to yield light hydrocarbons,[10,16,19] while the low Fe:C ratio phase $Fe_2C$ works at low temperatures (450 K) for producing $C_{5+}$ products.[11,12] Among the carbide phases, the intermediate Fe:C ratio phase, $Fe_5C_2$ phase, was most discussed in the literature, which appears to be the most active in producing $C_{5+}$ products at intermediate temperatures (540 K). For example, by introducing bromide as an inducing agent and $Fe(CO)_5$ as the precursor reagent, the Ma group[13] synthesized single-phase $\chi$-$Fe_5C_2$ nanoparticles, which were found to achieve a 39% initial CO conversion rate and ∼39% $C_{5+}$ hydrocarbon selectivity at high temperature (543 K, 3 MPa). The $\chi$-$Fe_5C_2$ phase increases the

Received: May 4, 2021
Published: July 17, 2021

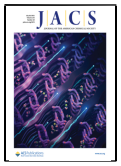





https://doi.org/10.1021/jacs.1c04624
J. Am. Chem. Soc. 2021, 143, 11109−11120

initial CO conversion and $C_{5+}$ product selectivity by 20% and 13% compared to the conventional catalyst reduced from $Fe_2O_3$. On the other hand, Chang et al.[9] reported that $Fe_7C_3$ displays three times higher intrinsic activity (TOF = $4.59 \times 10^{-2}$ $s^{-1}$) than $\chi$-$Fe_5C_2$ (TOF = $1.62 \times 10^{-2}$ $s^{-1}$) and $\varepsilon$-$Fe_2C$ (TOF = $1.50 \times 10^{-2}$ $s^{-1}$) at the reaction condition of 533−573 K. This was done by comparing three kinds of catalyst, i.e., $\chi$-$Fe_5C_2$, a $\chi$-$Fe_5C_2$ and $Fe_7C_3$ mixture, and a $\chi$-$Fe_5C_2$ and $\varepsilon$-$Fe_2C$ mixture, that were prepared by different pretreatment conditions (syngas, CO, or $H_2$) from iron oxide particles at 573 K.

Owing to the limitation of *in situ* experimental techniques, there is little information on the surface structure of carbide phases from experiment to date. Instead, a series of DFT calculations have been carried out on the surfaces of $Fe_4C$, $\theta$-$Fe_3C$, $\chi$-$Fe_5C_2$, and $\varepsilon$-$Fe_2C$ phases[20−24] by using the bulk-truncated surface structures. For example, on the $\chi$-$Fe_5C_2$ phase, Zhao et al.[20,21] found that the $\chi$-$Fe_5C_2$(100) surface has the lowest surface free energy ($\gamma \approx 1.80$ J/m$^2$) and $\chi$-$Fe_5C_2$(510) that was observed in experiment by XRD and high-resolution transmission electron microscope (HRTEM);[9,13,25,26] however, it has a high surface energy ($\gamma = 2.03$ J/m$^2$).[22]

As for the FTS mechanism on $FeC_x$ catalysts, most theoretical studies[23,24,27−34] were performed on simplified surface models, e.g., small unit cells without considering the possible surface reconstruction or neglecting the *in situ* coverage effects of adsorbates (e.g., carbon and hydrogen atoms) that are important to FTS kinetics.[35,36] This has led to diverse mechanisms for CO activation. Broos et al.[23] investigated the direct, H-assisted and C-assisted CO dissociation on the bulk-truncated surfaces of $\chi$-$Fe_5C_2$ and found the direct dissociation pathway on the Fe-$B_5$ site of $\chi$-$Fe_5C_2(11\bar{1})$ has the lowest barrier of 1.22 eV. However, He et al.,[32] after considering the coadsorption of H on different $\chi$-$Fe_5C_2$ surfaces, found that the H-assisted CO dissociation via an HCO intermediate on Fe-partially aggregated $\chi$-$Fe_5C_2$(010) has the lowest barrier (0.96 eV) with respect to the most stable CO adsorption site. On the other hand, Ozbek et al.[31] investigated the CO dissociation on $\chi$-$Fe_5C_2$(100) at different carbon coverages, and their results suggested the C vacancy mediated direct dissociation as the most feasible pathway with a barrier of 0.84 eV. Obviously, the reaction mechanism is sensitive to both the surface structures and the *in situ* coverages of C and H. How to cope with the high complexity of structures and reactions under FTS conditions has long been a problem too hard to solve by theory.

With the advent of the machine learning global exploration technique, here we aim to reveal the stable $FeC_x$ structures and CO activation mechanism under FTS conditions from first principles. The first quaternary Fe−C−H−O global neural network potential (G-NN) is now generated that allows the determination of the thermodynamics for $FeC_x$ bulk and surfaces via a fast global structure search. On the basis of thermodynamics criteria, we narrow the active sites to three surfaces, namely, $\chi$-$Fe_5C_2$(510), $\chi$-$Fe_5C_2$(111), and $\eta$-$Fe_2C$-(111), that have both a low surface energy and the ability to adsorb H atoms. On $\chi$-$Fe_5C_2$(510), which has the lowest surface energy among these surfaces, we demonstrate that CO activation can occur at the surface C-vacancy sites that are dynamically created via the surface C hydrogenation and diffusion.

## 2. METHODS

**2.1. SSW-NN Method.** All simulations based on the G-NN potential[37,38] were conducted by using LASP code[39] (large-scale atomic simulation with neural network potential, www.lasphub.com) developed in our group. The stochastic surface walking (SSW)[40,41] method was utilized for the global optimization that can automatically explore a multidimensional potential energy surface (PES) and to identify important structures and pathways as demonstrated in our previous work.[37,38,42,43] The G-NN potential follows the atom-centered NN potential architecture proposed by Behler and Parrinello,[44,45] where the input layer utilized the power-type structure descriptor (PTSD) designed by us previously.[38] Different from other machine learning potentials, the G-NN potential was generated by iteratively fitting the DFT global PES data obtained from the SSW global PES sampling, also known as the SSW-NN method, which typically speeds up PES calculations by 3−4 orders of magnitude compared with DFT. This allows for the efficient PES exploration at an accuracy comparable with DFT calculations.

We generated the quaternary-element Fe−C−H−O G-NN potential via the iterative self-learning scheme of the SSW-NN data set[37] by learning a large number of different compositions and configurations, including Fe bulk and surfaces, $FeC_x$ bulk and surfaces at different Fe:C ratios, and different atoms/molecules with C−H−O elements on these surfaces. These structures, being iteratively added into the data set during the G-NN potential generation, were selected from SSW-NN global optimization trajectories, either randomly or being distinct in structure as reflected by structure descriptors, or having a large energy deviation between G-NN and DFT results. More details on the G-NN generation and the SSW-NN method can be found in the SI. The final Fe−C−H−O training data set consists of 21 412 structures, which is openly accessible from the LASP Web site (see Web page link[46]), and a brief description of the data set in composition is also listed in SI Table S1. The Fe−C−H−O G-NN contains 124 524 parameters in total, with each element being represented by 305 PTSDs (111 two-body, 184 three-body, and 10 four-body PTSDs). The root-mean-square (RMS) errors for the energy and the force of the G-NN potential are 3.712 meV/atom and 0.119 eV/Å, respectively. The important low-energy structures from SSW-NN calculations have been further examined by using DFT calculations, and the benchmark results are detailed in SI Table S2 (XYZ coordinates are deposited in SI in a separate file), which showed that the energy RMS error is 2.28 meV/atom for important minima. The accuracy is good enough for the SSW global PES search to find low-energy minima.

**2.2. DFT Calculations.** All DFT calculations were performed by using the plane-wave VASP (Vienna Ab-initio Simulation Package) code,[47] where the electron−ion interaction is represented by the projector-augmented wave (PAW) potential. The exchange−correlation potential utilized was the GGA-PBE,[48] and the kinetic energy cutoff was 450 eV. The spin polarization has been also considered in all DFT calculations. The first Brillouin zone *k*-point sampling adopted the Monkhorst−Pack scheme with an automated mesh determined by 25 times the reciprocal lattice vectors. The energy and force criteria for convergence of the electron density and structure optimization were set at $5 \times 10^{-5}$ eV and 0.05 eV/Å, respectively. It should be mentioned that we have confirmed all important minima and pathways by DFT calculations, and thus, if otherwise specifically mentioned, *all energetics data reported in this work are from DFT calculations*.

**2.3. Surfaces and Reaction Modeling.** For surface and reaction calculations, the slab models utilized typically contain at least four Fe layers. To identify the global minima (GM) of $FeC_x$ surfaces, we started from a number of possible bulk truncated surfaces with both sides of the surface keeping the same termination. The SSW-NN global optimization were then utilized to find the GM, where the middle layers were fixed at the bulk-truncated positions and both sides of the surfaces were allowed to relax. This procedure was then repeated by adding extra or extracting surface C atoms from the low-energy surface candidates obtained from previous runs until no better surface configurations can be identified from SSW-NN.

Once the stable surface configuration was determined, we fixed the bottom $FeC_x$ layers and relaxed the top two surface layers together with adsorbed molecules for modeling the molecular adsorption and reactions. The double-ended surface walking (DESW) method[49,50] was utilized to locate the transition states (TS) for the reactions. This


https://doi.org/10.1021/jacs.1c04624
J. Am. Chem. Soc. 2021, 143, 11109−11120

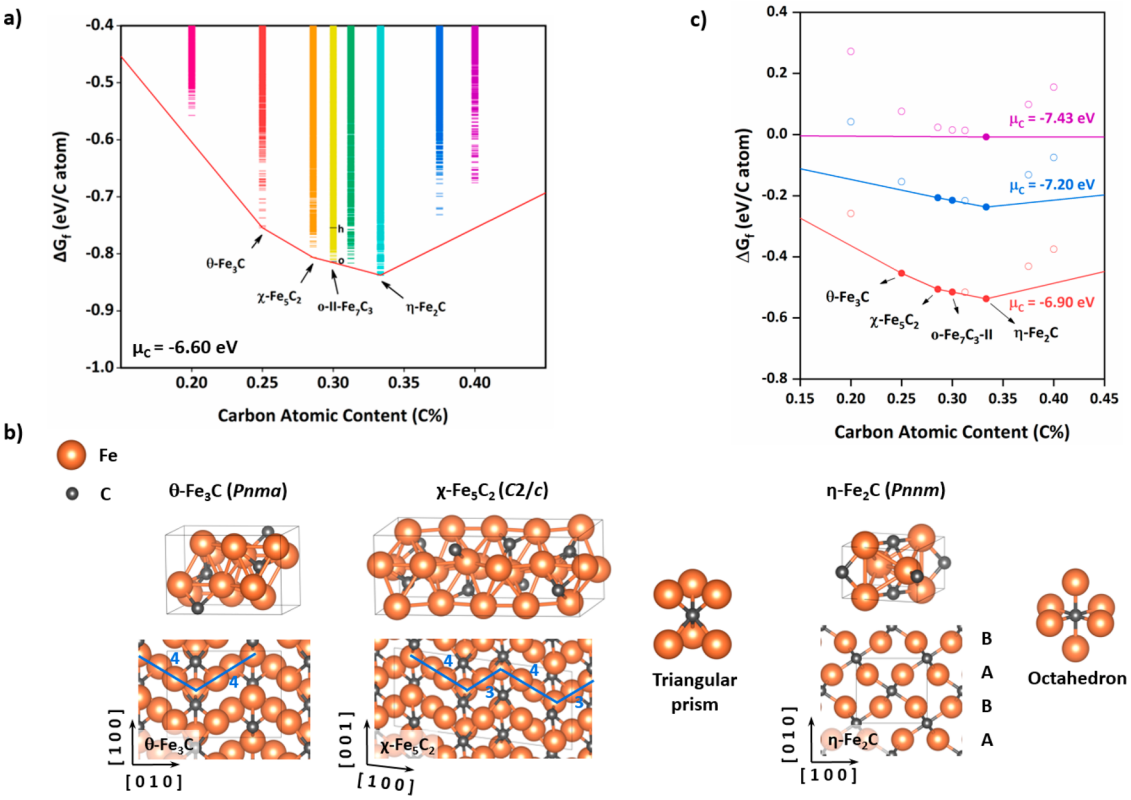


**Figure 1.** Thermodynamics and structures of bulk $FeC_x$ at different carbon atomic content. (a) Thermodynamics convex hull diagram for bulk $FeC_x$ referring to Fe (bcc phase) and $\mu_C = -6.60$ eV. The arrows specify the convex points. o-$Fe_7C_3$ and h-$Fe_7C_3$ are labeled by "o" and "h" with a black line. (b) Structures of the GM of $Fe_3C$ (*Pnma*, #62), $Fe_5C_2$ (*C*2/*c*, #15), and $Fe_2C$ (*Pnnm*, #58) and their Fe−C coordination pattern. Fe: orange, C: gray. (c) Thermodynamics convex hull diagram at three typical carbon chemical potentials ($\mu_C = -7.43$, −7.20, and −6.90 eV). Solid circle: convex point, hollow circle: concave point.

was achieved by driving two images from the initial state (IS) and final state (FS) toward each other via the consecutive adding of bias Gaussian potentials. After the path was connected, the constrained Broyden dimer (CBD) method[51,52] starting from the maximum energy point along the path was then utilized to locate the TSs, which were further confirmed by vibrational frequency calculations and the extrapolation optimization to the correct IS and FS (see for example Figure S7). All the pathways initially obtained from G-NN calculations were finally converged by DFT.

To analyze the diffusion ability of H and C on surfaces, we have performed a long-time molecular dynamics (MD) simulation up to 5 ns in the isothermal (NVT) ensemble with the Nosé−Hoover thermostat by using G-NN calculations. The Nosé−Hoover mass utilized was 100 eV·fs$^2$, and the time-step utilized was 0.5 fs. Two simulations with different temperatures were performed, i.e., 523 and 900 K. The unit cell for MD simulation contains a $p(2 \times 1)$ supercell with four Fe layers of $\chi$-$Fe_5C_2$(510) surface, i.e., 116 atoms in total.

## 3. RESULTS

**3.1. Thermodynamics of $FeC_x$ Bulk Phases.** The SSW-NN global optimization was first utilized to determine the thermodynamics of $FeC_x$ phases. Eight different Fe:C ratios (C %: 0.20−0.40), including $Fe_4C$, $Fe_3C$, $Fe_5C_2$, $Fe_7C_3$, $Fe_{2.2}C$, $Fe_2C$, $Fe_5C_3$, and $Fe_3C_2$, were considered, and their global PESs were explored in different supercells ranging from 16 to 64 atoms. In total, more than $10^6$ minima structures were visited for all $FeC_x$ phases with more than 30 000 minima collected in each supercell.

Under FTS conditions, the catalyst is in a rich C source (from reactant) environment. The stability of the $FeC_x$ phase can thus be evaluated by computing the exothermicity of entering to the Fe lattice per C atom, i.e., the free formation energy per carbon atom $\Delta G_f$ by referencing to the bulk Fe metal and the chemical potential of C ($\mu_C$) in the system in eq 1,

$$\Delta G_f(FeC_x) = [G(FeC_x) - G(Fe) - x\mu_C]/x \quad (1)$$

where $G(FeC_x)$ and $G(Fe)$ are the Gibbs free energy of the $FeC_x$ phase and Fe metal (bcc phase). The free energy of the solid bulk approximately equals the sum of the DFT total energy and the vibrational zero-point energy (ZPE) correction.[53] The $\mu_C$ can be derived from the FTS conditions, where the C in the catalyst is treated at the thermodynamics equilibrium with the mixture of reactant and product (e.g., CO, $H_2$, $C_2H_4$, and $H_2O$). Under FTS, we can define $\mu_C$ in a range with the upper bound from the reactant−catalyst equilibrium (∼10% CO conversion[14,54]) in eq 2 and the lower bound from the product−catalyst equilibrium (∼70% CO conversion[6]) in eq 3.

$$CO + H_2 \rightarrow C + H_2O,$$
$$\mu_C = \mu_{CO} + \mu_{H_2} - \mu_{H_2O} - E_C = -6.60 \text{ eV} \quad (2)$$

$$\frac{1}{2}C_2H_4 \rightarrow C + H_2,$$
$$\mu_C = \frac{1}{2}\mu_{C_2H_4} - \mu_{H_2} - E_C = -7.45 \text{ eV} \quad (3)$$

In eqs 2 and 3, $E_C$ is the energy of a reference free carbon atom from DFT, and $\mu_{CO}$, $\mu_{H_2}$, $\mu_{H_2O}$, and $\mu_{C_2H_4}$ are chemical potentials for CO, $H_2$, $H_2O$, and $C_2H_4$ gas phases in the typical FT


https://doi.org/10.1021/jacs.1c04624
J. Am. Chem. Soc. 2021, 143, 11109−11120

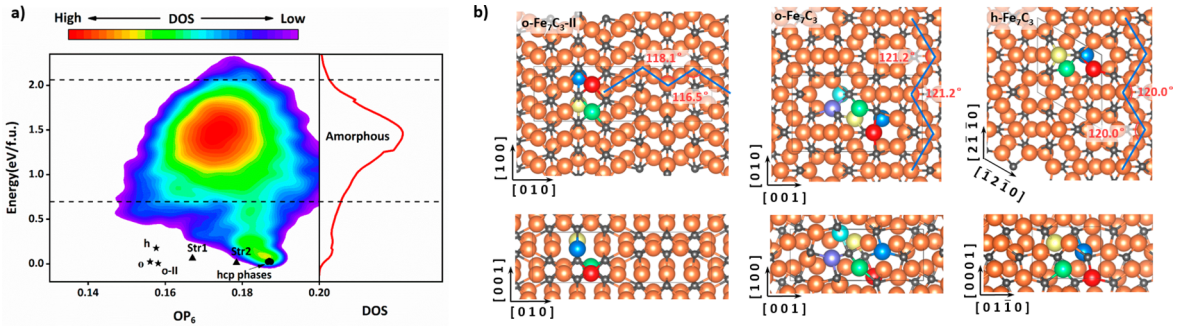


**Figure 2.** (a) Global PES contour plot for $Fe_7C_3$ using minima from SSW-NN. The *y* axis is the energy referring to the GM. $OP_6$: the structure order parameter with $l = 6$. Some representative structures are labeled by circles (hcp phases with octahedral Fe−C coordinations), triangles (phases with mixed octahedral and triangular prismatic Fe−C coordinations), and stars (o-$Fe_7C_3$-II, o-$Fe_7C_3$, and h-$Fe_7C_3$). (b) Comparison of the structures of o-$Fe_7C_3$-II (*Pnma*, #62, $a = 4.96$ Å, $b = 16.19$ Å, $c = 4.54$ Å), o-$Fe_7C_3$ (*Pnma*, #62, $a = 4.51$ Å, $b = 6.84$ Å, $c = 11.74$ Å), and h-$Fe_7C_3$ ($P6_3mc$, #186, $a = b = 6.85$ Å, $c = 4.45$ Å). Fe: orange, C: gray. Different layers of Fe atoms in o-$Fe_7C_3$-II, o-$Fe_7C_3$, and h-$Fe_7C_3$ are labeled with different colors (yellow, blue, green, red, cyan, and purple).

condition ($T = 523$ K, $P_{H_2} = 1.67$ MPa, $P_{CO} = 0.83$ MPa, $P_{C_2H_4} = 0.30$ MPa, and $P_{H_2O} = 0.09$ MPa).[21] The $\mu_C$ relevant to FTS is thus in the range of −7.45 to −6.60 eV from eqs 2 and 3. The high end $\mu_C = -6.6$ eV represents the low conversion stage of FTS, where the C from the reactant CO enters into solid-forming carbide phases, and the low end $\mu_C = -7.4$ eV indicates the FT products (mainly olefins) are in equilibrium with the C in carbide, corresponding to the typical steady state condition of FTS. In the following, we will analyze the thermodynamics of the $FeC_x$ phases in the range of $\mu_C$, −7.45 to −6.60 eV.

By using the GM for each composition, we plot the thermodynamics convex hull for $FeC_x$ phases in Figure 1a at the high end of $\mu_C$ (−6.60 eV), where the vertical axis represents $\Delta G_f$ and the horizontal axis represents the carbon atomic content, and the color bar in the figure illustrates the energy spectrum of distinct low-energy minima identified for each composition. It shows that at the early stage of FTS a number of Fe:C ratio phases below 3:1 can form; that is, there are four convex points at C% = 0.25, 0.29, 0.30, and 0.33, corresponding to four thermodynamically stable phases $Fe_3C$, $Fe_5C_2$, $Fe_7C_3$, and $Fe_2C$, respectively ($\Delta G_f = -0.75$, −0.81, −0.82, and −0.84 eV, respectively; also see SI Table S4 for all data). The low C% phase, e.g., $Fe_4C$, is found to be a biphase crystal mixing the Fe metal with the $Fe_3C$ phase (see SI Figure S1), which suggests the poor stability of $Fe_4C$ (concave point in Figure 1a) that prefers to decompose into $Fe_3C$ and Fe.

We note that the GMs of $Fe_3C$, $Fe_5C_2$, and $Fe_2C$ identified are the same as the known crystal phase $\theta$-$Fe_3C$ (*Pnma*, #62), $\chi$-$Fe_5C_2$ (*C*2/*c*, #15), and $\eta$-$Fe_2C$ (*Pnnm*, #58), respectively. These GM structures have also been identified previously by using the global optimization based on a genetic algorithm.[55] The GMs of $Fe_3C$ and $Fe_5C_2$ are well-defined since they are much lower in energy than the second lowest energy minimum, while there are nearly energy degenerate minima close to the GM for $Fe_7C_3$ bulk and, to a greater extent, for $Fe_2C$ bulk, as evident by its continuous energy spectrum in Figure 1a.

We now briefly overview the GM structures. The $\theta$-$Fe_3C$ and $\chi$-$Fe_5C_2$, as shown in Figure 1b, have a similar Fe sublattice, a distorted hcp pattern with zigzag close-packed planes. This main structural feature can be identified as viewed from the [001] direction of $\theta$-$Fe_3C$ and from the [010] of $\chi$-$Fe_5C_2$: there is a four-by-four (4−4) periodic pattern for each Fe zigzag layer (blue lines in Figure 1b) in $\theta$-$Fe_3C$, but a longer 4−3−4−3 pattern in $\chi$-$Fe_5C_2$. The C atoms then fill the interstitial sites of the Fe sublattice, having a triangular prismatic bonding pattern (see Figure 1b). The six Fe−C bond distances range from 1.96 to 2.00 Å in $\theta$-$Fe_3C$ and are slightly longer, 1.96−2.03 Å, in $\chi$-$Fe_5C_2$.

The GM for $Fe_7C_3$ is a new crystal structure (*Pnma*, #62), namely, o-$Fe_7C_3$-II phase, differing from the known h-$Fe_7C_3$ ($P6_3mc$, #186) and o-$Fe_7C_3$ (*Pnma*, #62) phases. The smallest unit cell of the o-$Fe_7C_3$-II phase contains 40 atoms, the same as the o-$Fe_7C_3$ phase but two times larger than the h-$Fe_7C_3$ phase. Their $\Delta G_f$ values from DFT (PBE) calculations are −0.82, −0.82, and −0.75 eV for o-$Fe_7C_3$-II, o-$Fe_7C_3$, and h-$Fe_7C_3$, respectively, showing two o-phases are nearly degenerate (the other DFT functionals have also been utilized to compare the stability of these phases, which yield the same energy ordering; see SI Table S5). The Fe sublattice of the o-$Fe_7C_3$-II phase is closer to those with lower carbon content phases ($\theta$-$Fe_3C$ and $\chi$-$Fe_5C_2$), but a longer periodic 3−3−4−3−3−4 zigzag pattern as viewed from the [001] direction (we will return to discuss $Fe_7C_3$ phases in the next subsection).

For $\eta$-$Fe_2C$, it has a rutile structure, where Fe atoms form the standard hcp sublattice and C atoms fill in half of the octahedral interstices alternatively (see Figure 1b). The Fe−C bond in the Fe−C octahedron of $\eta$-$Fe_2C$ is shorter compared to $\theta$-$Fe_3C$ and $\chi$-$Fe_5C_2$, being 1.94 Å for the axial bonds and 1.92 Å for the equatorial bonds. It should be mentioned that it is the $\varepsilon$-$Fe_2C$ phase that is characterized in the FT experiment, where the C position in the Fe sublattice is randomly distributed since there are a large number of vacant octahedral sites. From our global structure search, we found that the second lowest minimum in $Fe_2C$ with disordered C filling is only 5 meV in $\Delta G_f$ less stable than the GM. Considering the high temperature under FTS conditions (500 K), it is expected that the configuration entropy contribution can lead to the random distribution of C in the Fe sublattice of $Fe_2C$.

Finally, to take into account the variation of $\mu_C$ (−7.43 to −6.90 eV) under FTS conditions, we have replotted the thermodynamics convex diagram in Figure 1c to understand the stability trend of the carbide phases. We found that, not surprisingly, the $\mu_C$ value strongly influences the relative stability of the $FeC_x$ phases. As the $\mu_C$ changes to lower values, the high Fe:C ratio $FeC_x$ bulk phases are no longer the convex point. For example, the $\theta$-$Fe_3C$ is not stable any more *below* $\mu_C = -6.96$ eV. As shown in Figure 1c, at $\mu_C = -7.20$ eV the $\Delta G_f$ of $\theta$-$Fe_3C$ is −0.15 eV, but its transformation from $Fe_3C$ to Fe and $Fe_5C_2$ is


https://doi.org/10.1021/jacs.1c04624
J. Am. Chem. Soc. 2021, 143, 11109−11120

exothermic by 0.03 eV. Further decreasing $\mu_C$ to −7.43 eV, only the lowest Fe:C ratio carbide, $\eta$-$Fe_2C$, is a slightly more stable phase than Fe with $\Delta G_f = -0.01$ eV. This suggests that the $FeC_x$ phases will transform back to Fe below $\mu_C = -7.43$ eV.

Our thermodynamics analyses of bulk $FeC_x$ phases confirm that multiple $FeC_x$ phases grow under FTS conditions. While the $Fe_3C$ phase forms at the early stage of FTS when the conversion is low, the favorable bulk carbide phases should be $Fe_5C_2$, $Fe_7C_3$, and $Fe_2C$ at the typical steady state conditions where olefin is the major product of FTS. The whole FTS cycle may be regarded as C storage into carbide phases from reactants and the C release to hydrocarbon products from carbide phases.

**3.2. $Fe_7C_3$ Bulk Phases.** The presence of an $Fe_7C_3$ phase as characterized by XRD under FTS condition was first reported by Eckstrom and Adcock early in the 1940s.[56] Nevertheless, the difficulty in the synthesis of the pure carbide phase limited the clear assignment of its atomic positions. In the next 40 years, by comparing the XRD pattern with those of known crystal structures (e.g., $Cr_7C_3$, $Mn_7C_3$), several possible crystal structures for $Fe_7C_3$ were proposed, including h-$Fe_7C_3$[57] and o-$Fe_7C_3$.[58] In 1983, using selected area electron diffraction (SAED) to study the single crystals of $Fe_7C_3$, Audier et al.[59] confirmed that $Fe_7C_3$ was orthorhombic. However, the real structure of $Fe_7C_3$ under FTS remains elusive.

For the importance of the $Fe_7C_3$ bulk phase to FTS and a new o-II phase is identified as GM from SSW-NN, we are interested in analyzing the global PES of $Fe_7C_3$ for settling the structure puzzles on $Fe_7C_3$. From 2851 distinct minima of $Fe_7C_3$ bulk structures collected from SSW-NN data, we can plot the $E$−OP contour map for the global PES of $Fe_7C_3$ as shown in Figure 2a, where OP is the structure fingerprint using the distance-weighted Steinhart order parameter with the degree $l = 6$ ($OP_6$).[60] Also shown in Figure 2a (right panel) is the energy-projected density of states (DOS) curve, which provides a quick overview on the global PES to identify the amorphous structure zone that centers ∼1.5 eV per formula unit (f.u.) above the GM.

From the $E$−OP plot, we can readily distinguish different phases: the hcp phase region locates at $OP_6 = 0.18-0.19$ and the distorted hcp phases all have $OP_6 = 0.15-0.16$. We found that the majority of the $Fe_7C_3$ low-energy structures (<+0.15 eV/f.u. with respect to the GM) are the hcp phases with the local octahedral Fe−C coordination, while there are only two distorted hcp phases, i.e., the o-$Fe_7C_3$ and o-$Fe_7C_3$-II (GM), with purely triangular prismatic coordination. h-$Fe_7C_3$ is also the distorted hcp phase but 0.20 eV/f.u. above the GM. In between these two regions are located the structures with both octahedral and triangular prismatic Fe−C coordinations, e.g., Str1 and Str2 in Figure 2a (0.098 and 0.035 eV/f.u. above GM; their structures are shown in SI Figure S2).

Now we can have a close look at the three low-energy distorted hcp $Fe_7C_3$ phases. The similar zigzag close-packed planes are present in all phases, as guided by the blue lines in Figure 2b. The angles of these zigzag patterns are close, being alternately 116.5° and 118.1° in o-$Fe_7C_3$-II, 121.2° in o-$Fe_7C_3$, and 120.0° in h-$Fe_7C_3$. The Fe−C bond lengths are 1.95−2.04 Å for o-$Fe_7C_3$ and o-$Fe_7C_3$-II phases and 1.94−2.01 Å for h-$Fe_7C_3$. The vertical edges of the Fe−C triangular prism are all about 2.6 Å, being 2.58−2.59 Å in o-$Fe_7C_3$-II, 2.59−2.66 Å in o-$Fe_7C_3$, and 2.61 Å in h-$Fe_7C_3$.

The electronic structures of o-$Fe_7C_3$-II, o-$Fe_7C_3$, and h-$Fe_7C_3$ are quite similar. The magnetic moment is calculated to be 1.63, 1.71, and 1.67 $\mu_B$ per Fe for o-$Fe_7C_3$-II, o-$Fe_7C_3$, and h-$Fe_7C_3$ phases, respectively, which is highly quenched compared to the magnetic moment of bulk Fe metal (2.21 $\mu_B$ per Fe). All the $Fe_7C_3$ phases are still metallic, although the Fermi level states are mainly contributed by one type of spin electrons (spin-down). These states around the Fermi level are dominated by Fe 3d states, as reflected by the large overlap in the total DOS (black) and the projected DOS onto Fe 3d (red) in Figure 3a.

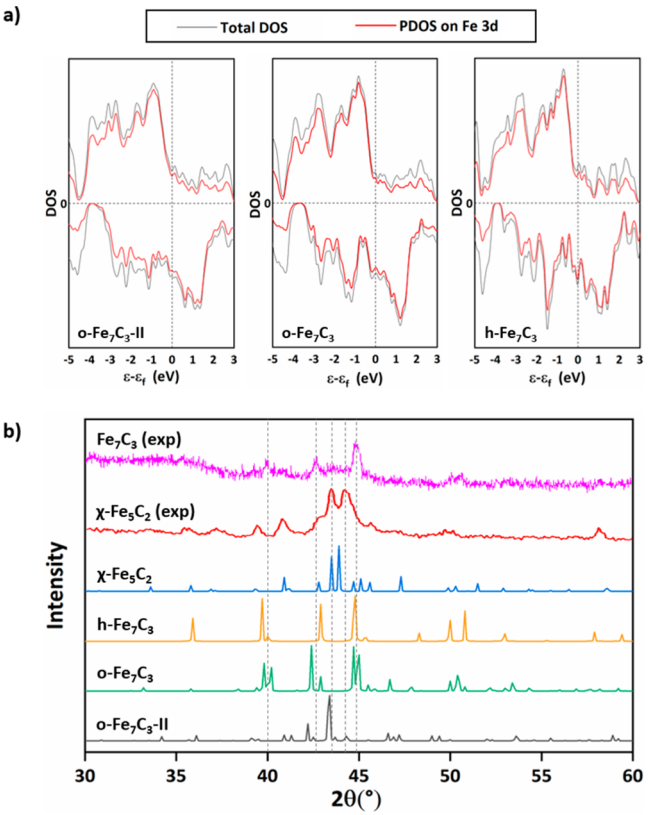


**Figure 3.** (a) Total DOS (black) and projected DOS on Fe 3d states (red) of o-$Fe_7C_3$-II, o-$Fe_7C_3$, and h-$Fe_7C_3$. (b) Simulated X-ray diffraction (Cu $K_{\alpha 1}$) patterns of o-$Fe_7C_3$-II, o-$Fe_7C_3$, h-$Fe_7C_3$, and $\chi$-$Fe_5C_2$. All simulated XRD patterns are shifted to lower angle by 0.5° in order to better compare the position of major peaks from the DFT lattice with that in experiments. The experimental XRD pattern of $Fe_7C_3$ is reproduced from ref 9. Copyright 2018 American Chemical Society. The experimental XRD pattern of $Fe_5C_2$ is reproduced from ref 13. Copyright 2012 American Chemical Society.

Despite the similarities of the three phases, they differ in the way the Fe sublattice is distorted from the perfect hcp lattice. As is shown in Figure 2b, the zigzag layers of o-$Fe_7C_3$-II are parallel to each another, exhibiting a lamellar form as $\theta$-$Fe_3C$ and $\chi$-$Fe_5C_2$. By contrast, the zigzag layers of o-$Fe_7C_3$ and h-$Fe_7C_3$ intersect with each other by additional interlayer Fe atoms and thus display the pattern of six-membered circles. The C sublattice is arranged in different ways in these two phases, a higher symmetry of $P6_3/mmc$ (#194) in h-$Fe_7C_3$ but a quite low symmetry of $Pnma$ (#62) in o-$Fe_7C_3$. By viewing from the close-packed line of Fe (e.g., [001] in o-$Fe_7C_3$), one can distinguish Fe atoms in different layers: as indicated by the color (yellow, blue, green, red, cyan, and purple) in Figure 2b, there are four, four, and six distinct Fe layers in o-$Fe_7C_3$-II, h-$Fe_7C_3$, and o-$Fe_7C_3$, respectively. In this sense, the crystal structure of o-$Fe_7C_3$ is the most complex.

To characterize the $Fe_7C_3$ phases and compare with the experimental data, we have also simulated XRD patterns of three


https://doi.org/10.1021/jacs.1c04624
J. Am. Chem. Soc. 2021, 143, 11109−11120

**Table 1. Properties of Low-Energy Surfaces in FTS**[a]

| | Fe:C ratio | $\gamma$ (J/m$^2$) | $\Delta E_f(C_v)$ (eV) | $G_{ad}$(H) (eV) | | $G_{ad}$(CO) (eV) |
|---|---|---|---|---|---|---|
| | | | | Fe−H | C−H | |
| $\theta$-$Fe_3C$ | | | | | | |
| $\theta$-$Fe_3C$(010) | 2.00 | **1.50** | 1.24 | 0.19 (b) | 0.19 | −0.65 (t) |
| $\theta$-$Fe_3C$(110)* | 2.00 | 2.01 | 0.87 | −0.41 (h) | 0.10 | −1.05 (h) |
| $\theta$-$Fe_3C$(001)* | 2.00 | 2.01 | 0.19 | −0.17 (h) | −0.62 | −0.53 (h) |
| $\chi$-$Fe_5C_2$ | | | | | | |
| $\chi$-$Fe_5C_2$(100) | 2.00 | **1.68** | 1.26 | 0.15 (b) | 0.20 | −0.66 (t) |
| $\chi$-$Fe_5C_2$(510)* | 2.00 | **1.75** | 1.08 | **−0.38 (h)** | **−0.10** | −1.06 (h) |
| $\chi$-$Fe_5C_2$(111) | 1.75 | **1.81** | 0.71 | **−0.18 (b)** | **−0.34** | −0.70 (t) |
| $\chi$-$Fe_5C_2$(010)* | 2.00 | 2.03 | 0.20 | −0.92 (h) | −0.99 | −1.39 (b) |
| o-$Fe_7C_3$-II | | | | | | |
| o-$Fe_7C_3$-II(010)* | 2.00 | **1.88** | 1.24 | 0.16 (b) | 0.21 | −0.66 (t) |
| o-$Fe_7C_3$-II(001)* | 2.00 | 2.07 | 0.28 | −0.55 (h) | −0.26 | −1.02 (h) |
| o-$Fe_7C_3$ | | | | | | |
| o-$Fe_7C_3$(101)* | 2.29 | 1.95 | 1.23 | −0.41 (h) | −0.28 | −0.75 (t) |
| o-$Fe_7C_3$(100) | 2.33 | 1.96 | 1.18 | −0.43 (h) | 0.03 | −0.99 (h) |
| $\eta$-$Fe_2C$ | | | | | | |
| $\eta$-$Fe_2C$(011) | 2.00 | **1.72** | 1.49 | 0.15 (h) | 0.34 | −0.57 (t) |
| $\eta$-$Fe_2C$(110) | 1.50 | **1.76** | 0.34 | 0.48 (b) | −0.35 | −0.67 (t) |
| $\eta$-$Fe_2C$(111)* | 2.00 | **1.83** | 0.47 | **−0.35 (h)** | **−0.05** | −0.79 (b) |
| $\eta$-$Fe_2C$(101)* | 2.00 | 2.07 | 1.30 | 0.15 (h) | 0.47 | −0.49 (t) |

[a] $\mu_C$ = −6.90 eV, reaction temperature at 523 K, and CO and $H_2$ pressures are at 0.83 and 1.67 MPa. Listed data include the surface Fe:C ratio, the surface free energy ($\gamma$), the C vacancy formation energy ($\Delta E_f(C_v)$), and the adsorption free energy ($G_{ad}$) of H (Fe-site and H-site) and CO. The asterisk indicates the surface is reconstructed. The adsorption site is indicated as t (top), b (bridge), and h (hollow site).

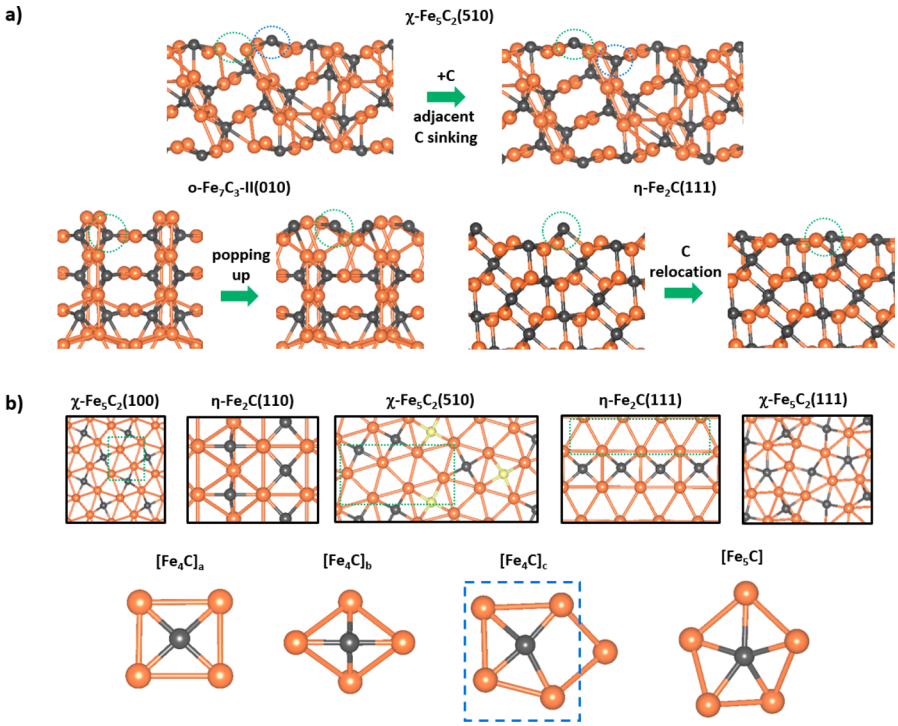


**Figure 4.** Structures of some important surfaces. (a) Reconstruction of some stable surfaces (side view). $\chi$-$Fe_5C_2$(510): extra C atoms occupy the 4-fold vacancy sites with one of the neighboring C atoms sinking. o-$Fe_7C_3$-II(010): the subsurface C atoms in the Fe-terminated surface pop up to the surface and the $[Fe_4C]_a$ squares are created. $\eta$-$Fe_2C$(111): the C atoms in the 3-fold site on the bulk-truncated surface relocate in the 4-fold vacancy sites. (b) Top views on eight stable surfaces ($\theta$-$Fe_3C$(010), o-$Fe_7C_3$-II(010), and $\eta$-$Fe_2C$(011) are the same as $\chi$-$Fe_5C_2$(100)). The green dotted lines label the 3-fold hollow sites on these surfaces. Four types of Fe−C coordination are also shown. Fe: orange, C: gray (upper) and yellow (lower).

$Fe_7C_3$ phases together with that of the $\chi$-$Fe_5C_2$ phase (Figure 3b). The typical XRD patterns for the $\chi$-$Fe_5C_2$ phase and $Fe_7C_3$ phase from experiments[9,13] are also depicted for comparison. The XRD of the $Fe_7C_3$ phase in experiment[9] shows multiple major peaks at 40.0°, 42.9°, and 44.9° and some other minor peaks at 42−45°. From our simulation, the major peaks of o-$Fe_7C_3$-II are at 43.9°, 42.7°, and 47.1°, which correspond to the crystal planes (071), (240), and (132), respectively. The major


https://doi.org/10.1021/jacs.1c04624
J. Am. Chem. Soc. 2021, 143, 11109−11120

peaks are at 45.5°, 45.2°, and 42.9° for (115), (131), and (202), respectively, in o-$Fe_7C_3$ and 45.3°, 43.4°, and 40.2° for (211), (102), and (210), respectively, in h-$Fe_7C_3$. Apparently, the XRD of o-$Fe_7C_3$-II has considerably fewer peaks than the other two phases and thus is apparently not consistent with the experimental data for $Fe_7C_3$, which show multiple major peaks at 40.0°, 42.9°, and 44.9°. However, we notice that the main peak of the o-$Fe_7C_3$-II phase at 43.9° in fact overlaps largely with that in the $\chi$-$Fe_5C_2$ phase that exhibits the major peaks at 43−45°.[13] Considering the close energetics of $Fe_7C_3$ and $Fe_5C_2$, the presence of the o-$Fe_7C_3$-II phase together with $\chi$-$Fe_5C_2$ cannot be ruled out under FTS conditions.

From XRD patterns and DFT energetics, we conclude that o-$Fe_7C_3$(energetically nearly degenerate with o-$Fe_7C_3$-II) is most likely the phase contributing to the characteristic XRD pattern of the $Fe_7C_3$ phase observed in experiment. The existence of o-$Fe_7C_3$-II is also likely since its XRD features can be masked by the $\chi$-$Fe_5C_2$ phase. The coexistence of o-$Fe_7C_3$-II and $\chi$-$Fe_5C_2$ may not be surprising because, as shown in Figure 1a and c, both of them are the convex points over a large $\mu_C$ range, −7.20 to −6.60 eV. The h-$Fe_7C_3$ phase, although its crystal structure is close to the known $Cr_7C_3$ phase, can be ruled out as the phase under FTS conditions due to its much poorer stability compared to the two o-phases.

**3.3. $FeC_x$ Surfaces.** Our next step is to identify the stable Fe carbide surfaces under FTS conditions. We have examined 30 different surfaces for five $FeC_x$ phases ($Fe_3C$, $Fe_5C_2$, $Fe_7C_3$ (o-II and o phases), and $Fe_2C$), including the low Miller index surfaces and the surfaces mentioned in the literature, as listed in SI Table S6. In our SSW-NN structure search, the different surface terminations and the surface reconstruction have been considered systematically, as described in Section 2, which may lead to the surface geometry deviating significantly from the bulk-truncated positions. In fact, it is quite common that extra C atoms are beneficial to stabilize the surface under FTS conditions. Similar to eq 1 for the bulk stability, we can measure the stability of surfaces using eq 4 to compute the surface free energy:

$$\gamma = [G_{\mathrm{sur\_FeCy}} - G_{\mathrm{FeCx}} - (y - x)\mu_C]/2A \quad (4)$$

where $G_{\mathrm{sur\_FeCy}}$ and $G_{\mathrm{FeCx}}$ denote the free energy of the surface and bulk, respectively, and the C atom contribution ($y$−$x$), if required, is to balance the equation with respect to the $\mu_C$. Our key results for the $FeC_x$ surfaces are summarized in Table 1 (also see SI Table S6 for other surfaces), which also include the C vacancy formation energy ($\Delta E_f(C_v)$) of the surface (the energy cost to create a C vacancy on the surface). All the data in Table 1 refer to $\mu_C$ = −6.90 eV (see Figure 1). We also computed the data at $\mu_C$ = −7.20 eV as detailed in SI Table S6, which yields a similar stability trend.

From Table 1, we can find that there are eight surfaces with lower surface energies, namely, $\theta$-$Fe_3C$(010), $\chi$-$Fe_5C_2$(100), $\chi$-$Fe_5C_2$(510), $\chi$-$Fe_5C_2$(111), o-$Fe_7C_3$-II(010), $\eta$-$Fe_2C$(011), $\eta$-$Fe_2C$(110), and $\eta$-$Fe_2C$(111). Their surface free energy are below 1.90 J/m$^2$, i.e., in the 1.50−1.88 J/m$^2$ range at $\mu_C$ = −6.90 eV. Among them, three surfaces, $\chi$-$Fe_5C_2$(510), o-$Fe_7C_3$-II(010), and $\eta$-$Fe_2C$(111), belong to the reconstructed surfaces. Figure 4a highlights the typical way of surface reconstruction. In $\chi$-$Fe_5C_2$(510), extra C atoms arrive to occupy the 4-fold Fe vacant sites that leads to the sinking of neighboring C atoms. The o-$Fe_7C_3$-II(010) with originally the Fe-dominated termination has the subsurface C atoms popping up to the surface to restore the Fe−C mixed termination. For $\eta$-$Fe_2C$(111), the surface C atoms relocate from the original 3-fold hollow sites of the bulk-truncated surface to the vacant 4-fold sites. Specifically, we summarize the major structural features of the eight low-energy surfaces as follows.

(i) **$\theta$-$Fe_3C$(010), $\chi$-$Fe_5C_2$(100), o-$Fe_7C_3$-II(010), and $\eta$-$Fe_2C$(011).** They are the lowest surface energy surfaces for each $FeC_x$ phase. Interestingly, all of them have the same surface pattern, as shown in the left panel of Figure 4b, that is, the same Fe:C ratio (=2) and the same four-coordinated planar C atoms ($[Fe_4C]_a$). The 3-fold Fe hollow sites are paired and separated by $[Fe_4C]_a$. For their high stability, it is difficult to create a C vacancy with $\Delta E_f(C_v)$ = 1.23−1.49 eV.

(ii) **$\eta$-$Fe_2C$(110).** It is the second lowest energy surface for the $\eta$-$Fe_2C$ phase, which can be truncated directly from the bulk without reconstruction. The surface Fe:C ratio is 1.50, being lower than the bulk. There are two types of C atoms on the surface, 0.33 monolayer (ML, with respect to surface Fe atoms) C atoms in $[Fe_4C]_a$ and 0.33 ML C atoms coordinated with four Fe atoms in a folded rectangular geometry ($[Fe_4C]_b$ in Figure 4b). It is easiest to create a C vacancy on $\eta$-$Fe_2C$(110) compared to other stable surfaces, $\Delta E_f(C_v)$ being only 0.34 eV.

(iii) **$\chi$-$Fe_5C_2$(510) and $\eta$-$Fe_2C$(111).** Both surfaces have the surface C atoms in an $[Fe_4C]_a$ pattern, but feature closely linked 3-fold Fe hollow sites, i.e., along [4−20−3] on $\chi$-$Fe_5C_2$(510) and along [1 0−1] on $\eta$-$Fe_2C$(111) (see dotted green rectangles in Figure 4b). For $\chi$-$Fe_5C_2$(510), the surface C atoms can be further divided into two types, the protruding ones (0.30 ML, protruding by 0.22−0.43 Å out of the Fe plane, gray balls in Figure 4b) and the sinking ones (0.20 ML, sinking by 0.61−0.66 Å, yellow balls). The $\Delta E_f(C_v)$ are 1.08 and 0.47 eV on $\chi$-$Fe_5C_2$(510) and $\eta$-$Fe_2C$(111), respectively.

(iv) **$\chi$-$Fe_5C_2$(111).** It has a complex surface geometry and relatively high surface energy (1.81 J/m$^2$). There are three types of surface C atoms, namely, $[Fe_4C]_b$, $[Fe_4C]_c$, and $[Fe_5C]$. In $[Fe_4C]_c$ (blue dashed line in Figure 4b), the C coordinates in a distorted $Fe_4$ square, where the Fe−Fe edges vary from 2.4 to 3.3 Å. In $[Fe_5C]$, the C coordinates with five Fe atoms in a quasi-planar pentagon. The number of different C atoms are 0.14, 0.29, and 0.14 ML in $[Fe_4C]_b$, $[Fe_4C]_c$, and $[Fe_5C]$, respectively. The $\Delta E_f(C_v)$ is 0.71 eV, in the middle of eight surfaces.

To summarize, we show that, despite the varied Fe:C ratio in bulk under FTS conditions, all stable surfaces tend to display the surface Fe:C ratio slightly below or about 2. This is done by proper surface reconstruction that can lead to the change in Fe:C composition. The stable surfaces as revealed by SSW-NN indicate the poorer stability of Fe-exposed metal sites and thus the general tendency to aggregate C onto the $FeC_x$ surfaces. Under FTS conditions, we expect that it is very unlikely to present Fe-$B_5$ sites[23] and the CO activation has to occur on the surfaces with the Fe-C mixed termination.

**3.4. CO Activation.** With the detailed knowledge on $FeC_x$ bulk and surfaces, we are finally at the position to understand how CO is activated, the key step in FTS. First, we determined the CO and H adsorption on $FeC_x$ surfaces, and the results are also listed in Table 1. We found that CO always prefers to adsorb at the Fe site and the adsorption free energy ($G_{ad}$) on different surfaces ranges from −0.49 to −1.39 eV (exothermic) under FTS conditions ($T$ = 523 K, $P_{CO}$ = 0.83 MPa). For the eight


https://doi.org/10.1021/jacs.1c04624
J. Am. Chem. Soc. 2021, 143, 11109−11120

most stable surfaces, CO can better adsorb on the 3-fold hollow site of $\chi$-$Fe_5C_2$(510) ($G_{ad}$ = −1.06 eV) and the bridge site of $\eta$-$Fe_2C$(111) ($G_{ad}$ = −0.79 eV), while chooses the top site on the other six stable surfaces ($G_{ad}$ = −0.57 to −0.70 eV). The C−O bond length is 1.20, 1.18, and 1.17 Å for the hollow site, bridge site, and top site adsorption configurations, respectively.

Different from CO adsorption, the dissociative adsorption of $H_2$ to the H atom is rather sensitive to the surface and can be either exothermic or endothermic. The H atom has two possible adsorption configurations, adsorbing on the Fe site or bonding with surface C (i.e., forming CH). Since the H atom supply is essential in FTS to produce long-chain hydrocarbons, we can first screen the active site for CO activation of FTS according to the following two criteria, i.e., (i) the exothermicity of $H_2$ dissociative adsorption; (ii) the mobility of H atoms on surface.

From Table 1, we can see that among the eight stable surfaces, four surfaces can adsorb H atoms ($G_{ad}$(H) < 0): except for $\eta$-$Fe_2C$(110), in which H can only bond with surface C, the other three surfaces, i.e., $\chi$-$Fe_5C_2$(510), $\chi$-$Fe_5C_2$(111), and $\eta$-$Fe_2C$-(111), allow H adsorption on Fe sites and also on C atoms. On these three surfaces, $G_{ad}$(H) on the Fe sites are −0.18 to −0.38 eV, indicating the exothermicity for dissociative $H_2$ adsorption. The H atom adsorbs on the 3-fold hollow site on $\chi$-$Fe_5C_2$ (510) and $\eta$-$Fe_2C$(111), and the bridge site on $\chi$-$Fe_5C_2$(111) (see SI Table S7). For $\eta$-$Fe_2C$(110), because the H atom adsorption on the Fe sites is 0.83 eV less stable than the H atom on a C atom, the H atoms only bond with C and the diffusion of H on the surface is kinetically slow. This largely rules out $\eta$-$Fe_2C$(110) as the active site for CO activation. We therefore narrow our search for the active site for CO activation of FTS to three $FeC_x$ surfaces, $\chi$-$Fe_5C_2$(510), $\chi$-$Fe_5C_2$(111), and $\eta$-$Fe_2C$(111), that can both dissociate $H_2$ exothermically and have a flat PES for H on both Fe sites and C sites.

By performing long-time MD simulations, we have further examined the mobility of H atoms on $\chi$-$Fe_5C_2$(510) at 523 K by putting two H atoms initially at Fe sites and C sites. In a 5 ns simulation, the H atoms generally remain around the initial sites, as shown in the trajectory in SI Figure S6. The H atoms on the Fe sites can diffuse over a larger area covering several nearby Fe atoms, but the H atoms on the C sites remain nearly intact, apparently because of the higher barrier of CH bond breaking (i.e., 0.62 eV from our DFT calculations). This confirms that the H diffusion on $\chi$-$Fe_5C_2$(510) needs to be activated: a 5 ns MD simulation at 523 K still cannot capture the continuous H diffusion over the whole surface. In fact, with the increase of temperature in MD, i.e., 900 K, we have observed the fast H diffusion, both on Fe sites and C sites, over the whole surface.

To demonstrate this, we plotted the radial distribution functions (RDF), $g(r)$, of H atoms from the final 2 ns trajectory at 523 and 900 K, respectively, as shown in Figure 5. The $g(r)$ is computed as eq 5:

$$g_{H-X}(r) = \frac{V}{N_X} \frac{\frac{1}{N_H}\sum_{i=1}^{N_H} n_{X_i}}{4\pi r^2 \Delta r} \quad (5)$$

where X represents the surface Fe and C and $n_{Xi}$ is the number of X situated in between the distance $r$ to $r + \Delta r$ from the centering H atom. All $g(r)$ are normalized by dividing the total number of centering H atoms and the number of X ($N_X$) in the slab and the volume of the slab ($V$). The RDFs for H−X at both 523 K (blue line) and 900 K (orange line) show the peak at a distance of ∼1.8 Å, which corresponds to the Fe−H bond length. The larger Fe−H peak at 900 K indicates H atoms appear more broadly on Fe

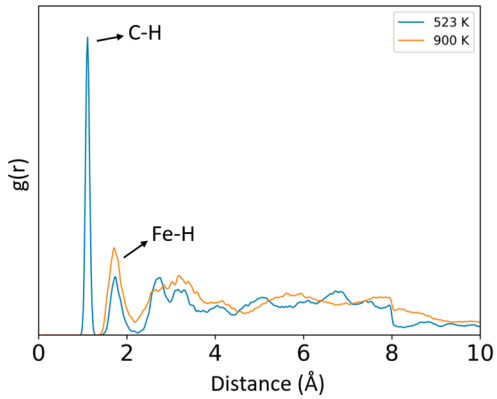


**Figure 5.** Radial distribution functions, $g(r)$, from 5 ns MD trajectories for surface H atoms at 523 K (blue) and 900 K (orange), respectively. The first bonding shell of H is dominated by C (forming CH) at 523 K and switches to Fe at 900 K.

sites at higher temperatures. Furthermore, the RDF at 523 K shows a sharp peak at a distance around 1.1 Å, which corresponds to the C−H bond length, indicating the trapping of H at the C site. The C−H peak is absent in the RDF at 900 K, reflecting H atoms diffuse rapidly on the Fe sites. Our MD results show that once the H bonds with the surface C atoms, the diffusion of H atom slows due to the need to break the local C−H bond, which confirms the importance of H adsorption on Fe sites.

We then focus on the CO activation on $\chi$-$Fe_5C_2$(510), which has the lowest surface free energy among these three surfaces. The overall free energy barrier is 1.11 eV for CO activation, as shown in the lowest energy profile for $\chi$-$Fe_5C_2$(510) in Figure 6a. The free energy is computed as our previous work,[61,62] where the ZPE is added and the entropy of gas phase molecules are corrected ($T$ = 523 K, $P$ = 2.5 MPa, $H_2$/CO = 2:1). The CO activation can be separated into two parts, i.e., the C vacancy formation and the CO dissociation over the C vacancy. It should be mentioned that the other reaction mechanisms, such as CO direct dissociation and H-assisted and C-assisted CO dissociation in the absence of a surface C vacancy, have much higher reaction barriers (above 2.2 eV) and thus can be ruled out (see SI Figure S8). In the following, we elaborate the reaction on the $\chi$-$Fe_5C_2$(510) surface in detail.

The reaction starts by the dissociative adsorption of $H_2$ onto the 3-fold hollow sites, which is a barrierless reaction exothermically by 0.74 eV (2H* in Figure 6a). A surface H atom then reacts with a nearby surface C atom in $[Fe_4C]_a$, which needs to overcome a barrier of 0.86 eV (TS1 in Figure 6b). The formation of CH is endothermic by 0.24 eV ($CH^*_{Cv}$ in Figure 6b). Then, the CH in the 4-fold site diffuses out to the nearby 3-fold hollow site, which leaves a C vacancy. The CH diffusion has a barrier of 0.69 eV (TS2 in Figure 6b) and is endothermic by 0.27 eV (CH* + $C_v$ in Figure 6b). Then, a coming CO molecule adsorbs at the C vacancy with an adsorption energy of 0.83 eV ($CO^*_{Cv}$ in Figure 6b, which is slightly less stable than CO at the nearby hollow site (−0.86 eV)). Finally, CO dissociation occurs with a barrier of 1.11 eV, which heals the C-vacancy site and produces an O atom nearby. At the TS of CO dissociation (TS3 in Figure 6b), the C−O bond distance increases from 1.22 Å in the adsorbed CO molecule to 1.72 Å, where the O-end evolves new bonding with the adjacent three Fe atoms. In the pathway, CO bond breaking is the rate-determining step (Figure 6a).


https://doi.org/10.1021/jacs.1c04624
J. Am. Chem. Soc. 2021, 143, 11109−11120

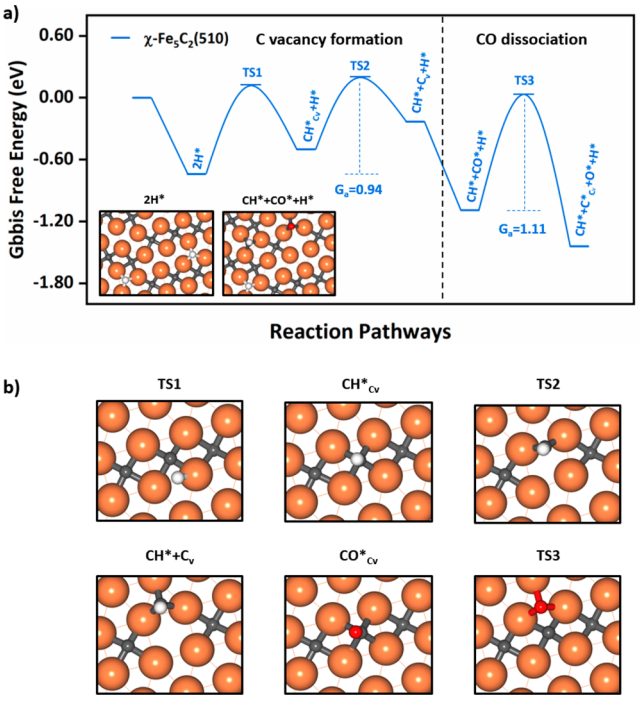


**Figure 6.** (a) Free energy profile for the lowest energy CO activation pathway mediated by the surface carbon vacancy. The reaction condition is set at $T$ = 523 K, $P$ = 2.5 MPa, $H_2$/CO = 2:1 for computing the free energies. The asterisk indicates the adsorption state. $C_v$ denotes the carbon vacancy on the surface. (b) Enlarged local view for the structure snapshots along the pathway in (a). Fe: orange, C: gray, H: white, O: red.

It might be mentioned that we have also considered the other reaction possibility for CH hydrogenation to $CH_2$, $CH_3$, and finally to $CH_4$ at the 4-fold site. It is found that the reaction from CH to $CH_2$, $CH_3$, and $CH_4$ is kinetically difficult, with the barrier being 1.10, 1.50, and 1.78 eV. The overall barrier for the diffusion of $CH_2$ and $CH_3$ out of the 4-fold site is also less favorable compared to that of CH diffusion. These results are detailed in SI Figure S9.

## 4. DISCUSSIONS

**4.1. CO Activation and the Role of a Surface Carbon Vacancy.** CO activation was long regarded to be the key step in FTS. Previous theoretical studies[22,23,31−34] have suggested four possible mechanisms: (i) direct dissociation over Fe sites; (ii) H-assisted CO dissociation on Fe sites; (iii) (H)/C-assisted CO dissociation on C sites; (iv) C-vacancy-mediated direct dissociation. Mechanism (i) has a relatively high barrier (1.62 eV on $\chi$-$Fe_5C_2(11\bar{1})$[23]), but the exposure of the Fe-$B_5$ site[23,33] can reduce the barrier to 1.22 eV. The major problem of Fe-$B_5$ site catalyzed CO dissociation is that these sites are significantly less stable compared to the $FeC_x$ surface, as shown from our surface structure exploration and also by Zhao et al.[21] The surfaces under FTS are generally covered by C atoms with a low Fe:C ratio (≤2) from our work. Although the H-assisted (via CHO, COH) and (H)/C-assisted (via CCO, CCHO, CCOH) CO dissociation pathways were also suggested previously, this work, by using the stable surfaces under FTS, shows that these mechanisms have too high barriers (>2.2 eV).

A number of previous studies[23,32,63] have compared the CO dissociation on different $FeC_x$ surfaces, which generally did not consider the surface structure under FTS as pinned by appropriate $\mu_C$.[31,34,64] Despite the limitation of the structure model, these studies have noticed that the best CO dissociation might involve the 4-fold Fe hollow sites that are present on many $FeC_x$ surfaces. In particular, the $\chi$-$Fe_5C_2$(510) as the active site for FTS has been suggested from experiment, which can be present as the dominant facet in the cylindrical $Fe_5C_2$ catalyst.[26,65] The theoretical calculations on the unreconstructed $\chi$-$Fe_5C_2$(510) where the 4-fold vacant Fe sites are naturally available reported the CO dissociation barriers of 1.18, 0.99, and 1.17 eV by He et al.,[32] Zhang et al.,[29] Chen et al.,[63] respectively. Based on thermodynamics analyses, we now show that $\chi$-$Fe_5C_2$(510) can undergo surface reconstruction, and thus all 4-fold vacant sites of Fe are filled in the most stable configuration. Under FTS, the C vacancy can then be dynamically created with a barrier of 0.94 eV (TS2 in Figure 6a), and the CO dissociation reaction can occur with a barrier of 1.11 eV (TS3 in Figure 6a).

For the importance of a C vacancy, it is essential to discuss how the carbon vacancy is created. One of the possibilities is that the surface C atoms are mobile under FTS conditions, which can diffuse out from the hollow site and create the vacancy. This possibility is, however, unlikely according to our results. First, the C vacancy is thermodynamically difficult to create on the lowest surface energy surfaces, where the $\Delta E_f(C_v)$ is more than 1.23 eV (see Table 1). Second, for the minority surface facets with smaller $\Delta E_f(C_v)$, the diffusion of surface C atoms is also kinetically difficult. From our MD simulation, the surface C atoms do not diffuse on the reconstructed $\chi$-$Fe_5C_2$(510) surface in the 5 ns MD simulation at 523 K. This is consistent with the calculated energy profile for the C atoms moving out from the hollow site to the sites above the surface, which is endothermic with a high barrier (1.26 eV, see SI Figure S9). Instead of the direct C diffusion, we show that the pathway for the creation of the C vacancy by hydrogenation to CH is more favorable, being 0.94 eV on the reconstructed $\chi$-$Fe_5C_2$(510) (Figure 6a). This suggests that the C vacancy can be created dynamically on the minority surface facets via the hydrogenation reaction during FTS. Although the hydrogenation is kinetically feasible, we expect that the surface C vacancy sites under FTS conditions would be low in concentration due to the overall endothermicity in forming a CH and a $C_v$.

As for the exact concentration of C vacancies, to the best our knowledge, there is no direct quantitative data from experiment. The previous kinetics modeling based on experimental kinetics data by van Steen et al.[66] and Sarkari et al.[67] have suggested that under FTS the catalyst surface is covered by C, implying the low concentration of C vacancies. Most of the kinetics modeling[35,67,68] fitting the low-pressure experiment data also show that the overall rate of FTS is sensitive to $H_2$ pressure (in the reaction order of 0.25−1) and the $H_2$ gas plays an important role in reacting with surface C to form organic molecules. In their model,[66,67] the CH formation via surface C and surface H is proposed to be the rate-determining step in the low-pressure experiment ($H_2$ pressure below 6 bar). The kinetics model is consistent with our results that the C vacancies as the reaction center are needed for FTS, which can only be created dynamically during FTS by the hydrogenation of surface C. The positive order of $H_2$ pressure is not due to H-assisted reaction channels via CHO or COH, but, instead, may well be related to its role in increasing the H coverage to compete with CO adsorption since CO is found to adsorb more strongly than the H atom (Table 1). Once the C vacancy is available, the CO


https://doi.org/10.1021/jacs.1c04624
J. Am. Chem. Soc. 2021, 143, 11109−11120

can dissociate directly at the site, as found by us and also reported by others on the unreconstructed $FeC_x$ surfaces.[34,64]

**4.2. H Coverage under FTS.** Our results show that the H atom has quite different adsorption energies on different surfaces and thus it should distribute inhomogeneously on catalysts. In particular, on the most stable surfaces, i.e., $\theta$-$Fe_3C(010)$, $\chi$-$Fe_5C_2(100)$, o-$Fe_7C_3$-II(010), and $\eta$-$Fe_2C(011)$, the H free adsorption energy is generally positive, indicating the most stable surfaces have very low H coverage, and consequently the C-vacancy sites are unlikely to be created. On the less stable surfaces with exothermic H adsorption free energy, as represented by $\chi$-$Fe_5C_2(510)$, the H adsorption free energy is up to −0.38 eV on Fe sites and the formation of CH by reacting H with nearby surface C is kinetically possible (Figure 6). This offers the possibility for C vacancy creation on $\chi$-$Fe_5C_2(510)$, $\chi$-$Fe_5C_2(111)$, and $\eta$-$Fe_2C(111)$ surfaces.

Experimentally, there are few data on the *in situ* H coverage under FTS. Xie et al.[36] reported that H coverage is 1−4 ML (with respect to surface C atoms) for iron-based catalysts at methanation conditions ($H_2$/CO = 10). The catalyst is only partially carburized (∼20%). We found that on the $FeC_x$ surfaces the saturation H coverage is generally lower than 1 ML with respect to surface C atoms. For example, on $\chi$-$Fe_5C_2(510)$, the saturation H coverage is no more than 0.90 ML when the differential $G_{ad}(H)$ goes positive with respect to the gas phase $H_2$ (Figure S4). We expect that under FTS conditions, the H coverage should be even lower due to the competitive coadsorption of CO reactant and hydrocarbon products.

## 5. CONCLUSION

This work utilizes machine learning based global PES exploration to identify the active site for CO activation in FTS. By exploring globally structures from the bulk to surfaces and to reactions, we identify three low-energy surfaces that belong to two $FeC_x$ bulk phases, i.e., $\chi$-$Fe_5C_2(510)$, $\chi$-$Fe_5C_2(111)$, and $\eta$-$Fe_2C(111)$ for FT conversion. We show that under FTS conditions the $FeC_x$ surfaces are dynamic, involving not only structure reconstruction but also the change of composition, and thus the surface Fe:C ratio may well not be the same as that of bulk phases. Importantly, the most stable surfaces, the majority surface facets, generally adopt the same $Fe_2C$ surface pattern but are inactive for FTS due to the endothermic H adsorption and the large endothermicity in creating the C vacancy. Instead, CO activation occurs via a direct dissociation pathway over the surface C vacancies on the minority surface facets, such as the reconstructed $\chi$-$Fe_5C_2(510)$, where H atoms can adsorb exothermically on the exposed Fe sites and the C vacancy formation is thermodynamically less endothermic. Since FTS represents one of the most complex heterogeneous catalytic systems with both rich catalyst phases and multiple product selectivity, the advance achieved here demonstrates that the first-principles solution of complex catalytic problems under reaction conditions is now accessible with the advent of machine learning global optimization.

## ■ ASSOCIATED CONTENT

### Supporting Information

The Supporting Information is available free of charge at https://pubs.acs.org/doi/10.1021/jacs.1c04624.

Methods: Construction of Fe−C−H−O quaternary G-NN potential; benchmark of G-NN potential against DFT calculations; calculations of carbon chemical potential ($\mu_C$); $FeC_x$ bulk phase; $FeC_x$ surfaces; adsorption sites for H/CO; H and C diffusion on the surface from molecular dynamics; other CO activation pathways and $CH_x$ diffusion pathway (PDF)

*xyz* coordinates for all the structures mentioned in SI Table S2 and Figure 6a (TXT)

## ■ AUTHOR INFORMATION


### Corresponding Authors

**Cheng Shang** − *Collaborative Innovation Center of Chemistry for Energy Material, Shanghai Key Laboratory of Molecular Catalysis and Innovative Materials, Key Laboratory of Computational Physical Science, Department of Chemistry, Fudan University, Shanghai 200433, China;* orcid.org/0000-0001-7486-1514; Email: cshang@fudan.edu.cn

**Zhi-Pan Liu** − *Collaborative Innovation Center of Chemistry for Energy Material, Shanghai Key Laboratory of Molecular Catalysis and Innovative Materials, Key Laboratory of Computational Physical Science, Department of Chemistry, Fudan University, Shanghai 200433, China;* orcid.org/0000-0002-2906-5217; Email: zpliu@fudan.edu.cn

### Author

**Qian-Yu Liu** − *Collaborative Innovation Center of Chemistry for Energy Material, Shanghai Key Laboratory of Molecular Catalysis and Innovative Materials, Key Laboratory of Computational Physical Science, Department of Chemistry, Fudan University, Shanghai 200433, China*

Complete contact information is available at: https://pubs.acs.org/10.1021/jacs.1c04624


### Notes

The authors declare no competing financial interest.

## ■ ACKNOWLEDGMENTS

This work was supported by the National Key Research and Development Program of China (2018YFA0208600) and the National Science Foundation of China (91945301, 21533001, 22033003, 91645201, and 91745201).

## ■ REFERENCES


(1) de Smit, E.; Swart, I.; Creemer, J. F.; Hoveling, G. H.; Gilles, M. K.; Tyliszczak, T.; Kooyman, P. J.; Zandbergen, H. W.; Morin, C.; Weckhuysen, B. M.; de Groot, F. M. Nanoscale chemical imaging of a working catalyst by scanning transmission X-ray microscopy. *Nature* **2008**, *456*, 222−225.

(2) de Smit, E.; van Schooneveld, M. M.; Cinquini, F.; Bluhm, H.; Sautet, P.; de Groot, F. M.; Weckhuysen, B. M. On the surface chemistry of iron oxides in reactive gas atmospheres. *Angew. Chem., Int. Ed.* **2011**, *50*, 1584−1588.

(3) Li, Y. J.; Li, Z. S.; Ahsen, A.; Lammich, L.; Mannie, G. J. A.; Niemantsverdriet, J. W. H.; Lauritsen, J. V. Atomically Defined Iron Carbide Surface for Fischer−Tropsch Synthesis Catalysis. *ACS Catal.* **2019**, *9*, 1264−1273.

(4) Galvis, H. M. T.; Bitter, J. H.; Davidian, T.; Ruitenbeek, M.; Dugulan, A. I.; de Jong, K. P. Iron Particle Size Effects for Direct Production of Lower Olefins from Synthesis Gas. *J. Am. Chem. Soc.* **2012**, *134*, 16207−16215.

(5) Galvis, H. M. T.; Bitter, J. H.; Khare, C. B.; Ruitenbeek, M.; Dugulan, A. I.; de Jong, K. P. Supported Iron Nanoparticles as Catalysts for Sustainable Production of Lower Olefins. *Science* **2012**, *335*, 835−838.

(6) Santos, V. P.; Wezendonk, T. A.; Jaen, J. J. D.; Dugulan, A. I.; Nasalevich, M. A.; Islam, H. U.; Chojecki, A.; Sartipi, S.; Sun, X.;

Hakeem, A. A.; Koeken, A. C. J.; Ruitenbeek, M.; Davidian, T.; Meima, G. R.; Sankar, G.; Kapteijn, F.; Makkee, M.; Gascon, J. Metal organic framework-mediated synthesis of highly active and stable Fischer−Tropsch catalysts. *Nat. Commun.* **2015**, *6*, 6451.

(7) Lyu, S.; Wang, L.; Li, Z.; Yin, S. K.; Chen, J.; Zhang, Y. H.; Li, J. L.; Wang, Y. Stabilization of epsilon-iron carbide as high-temperature catalyst under realistic Fischer−Tropsch synthesis conditions. *Nat. Commun.* **2020**, *11*, 6219.

(8) Xu, Y. F.; Li, X. Y.; Gao, J. H.; Wang, J.; Ma, G. Y.; Wen, X. D.; Yang, Y.; Li, Y. W.; Ding, M. Y. A hydrophobic FeMn@Si catalyst increases olefins from syngas by suppressing C1 by-products. *Science* **2021**, *371*, 610−613.

(9) Chang, Q.; Zhang, C.; Liu, C.; Wei, Y.; Cheruvathur, A. V.; Dugulan, A. I.; Niemantsverdriet, J. W.; Liu, X.; He, Y.; Qing, M.; Zheng, L.; Yun, Y.; Yang, Y.; Li, Y. Relationship between Iron Carbide Phases (ε-Fe2C, Fe7C3, and ε-Fe5C2) and Catalytic Performances of Fe/SiO2 Fischer−Tropsch Catalysts. *ACS Catal.* **2018**, *8*, 3304−3316.

(10) Qiu, T.; Wang, L.; Lv, S.; Sun, B. L.; Zhang, Y. H.; Liu, Z. N.; Yang, W. M.; Li, J. L. SAPO-34 zeolite encapsulated Fe3C nanoparticles as highly selective Fischer−Tropsch catalysts for the production of light olefins. *Fuel* **2017**, *203*, 811−816.

(11) Xu, K.; Sun, B.; Lin, J.; Wen, W.; Pei, Y.; Yan, S.; Qiao, M.; Zhang, X.; Zong, B. epsilon-Iron carbide as a low-temperature Fischer−Tropsch synthesis catalyst. *Nat. Commun.* **2014**, *5*, 5783.

(12) Wang, P.; Chen, W.; Chiang, F. K.; Dugulan, A. I.; Song, Y. J.; Pestman, R.; Zhang, K.; Yao, J. S.; Feng, B.; Miao, P.; Xu, W. N.; Hensen, E. J. M. Synthesis of stable and low-CO2 selective epsilon-iron carbide Fischer−Tropsch catalysts. *Sci. Adv.* **2018**, *4*, No. eaau2947.

(13) Yang, C.; Zhao, H.; Hou, Y.; Ma, D. Fe5C2 nanoparticles: a facile bromide-induced synthesis and as an active phase for Fischer−Tropsch synthesis. *J. Am. Chem. Soc.* **2012**, *134*, 15814−15821.

(14) Zhao, H.; Liu, J.-X.; Yang, C.; Yao, S.; Su, H.-Y.; Gao, Z.; Dong, M.; Wang, J.; Hou, Y.; Li, W.-X.; Ma, D. Synthesis of Iron-Carbide Nanoparticles: Identification of the Active Phase and Mechanism of Fe-Based Fischer−Tropsch Synthesis. *CCS Chem.* **2020**, *2*, 2712−2724.

(15) de Smit, E.; Weckhuysen, B. M. The renaissance of iron-based Fischer−Tropsch synthesis: on the multifaceted catalyst deactivation behaviour. *Chem. Soc. Rev.* **2008**, *37*, 2758−2781.

(16) de Smit, E.; Cinquini, F.; Beale, A. M.; Safonova, O. V.; van Beek, W.; Sautet, P.; Weckhuysen, B. M. Stability and Reactivity of epsilon-chi-theta Iron Carbide Catalyst Phases in Fischer−Tropsch Synthesis: Controlling mu(c). *J. Am. Chem. Soc.* **2010**, *132*, 14928−14941.

(17) Lyu, S.; Liu, C.; Wang, G.; Zhang, Y.; Li, J.; Wang, L. Structural evolution of carbon in an Fe@C catalyst during the Fischer−Tropsch synthesis reaction. *Catal. Sci. Technol.* **2019**, *9*, 1013−1020.

(18) Zhuo, O.; Yang, L. J.; Gao, F. J.; Xu, B. L.; Wu, Q.; Fan, Y. N.; Zhang, Y.; Jiang, Y. F.; Huang, R. S.; Wang, X. Z.; Hu, Z. Stabilizing the active phase of iron-based Fischer−Tropsch catalysts for lower olefins: mechanism and strategy. *Chem. Sci.* **2019**, *10*, 6083−6090.

(19) Herranz, T.; Rojas, S.; Perez-Alonso, F. J.; Ojeda, M.; Terreros, P.; Fierro, J. L. G. Genesis of iron carbides and their role in the synthesis of hydrocarbons from synthesis gas. *J. Catal.* **2006**, *243*, 199−211.

(20) Zhao, S.; Liu, X.-W.; Huo, C.-F.; Li, Y.-W.; Wang, J.; Jiao, H. Surface morphology of Hägg iron carbide (ε-Fe5C2) from ab initio atomistic thermodynamics. *J. Catal.* **2012**, *294*, 47−53.

(21) Zhao, S.; Liu, X.-W.; Huo, C.-F.; Li, Y.-W.; Wang, J.; Jiao, H. Determining surface structure and stability of ε-Fe2C, ε-Fe5C2, θ-Fe3C and Fe4C phases under carburization environment from combined DFT and atomistic thermodynamic studies. *Catalysis, Structure & Reactivity* **2015**, *1*, 44−60.

(22) Pham, T. H.; Duan, X.; Qian, G.; Zhou, X.; Chen, D. CO Activation Pathways of Fischer−Tropsch Synthesis on ε-Fe5C2 (510): Direct versus Hydrogen-Assisted CO Dissociation. *J. Phys. Chem. C* **2014**, *118*, 10170−10176.

(23) Broos, R. J. P.; Zijlstra, B.; Filot, I. A. W.; Hensen, E. J. M. Quantum-Chemical DFT Study of Direct and H- and C-Assisted CO Dissociation on the chi-Fe5C2 Hagg Carbide. *J. Phys. Chem. C* **2018**, *122*, 9929−9938.

(24) Broos, R. J. P.; Klumpers, B.; Zijlstra, B.; Filot, I. A. W.; Hensen, E. J. M. A quantum-chemical study of the CO dissociation mechanism on low-index Miller planes of θ-Fe3C. *Catal. Today* **2020**, *342*, 152−160.

(25) Retief, J. J. Powder diffraction data and Rietveld refinement of Hagg-carbide, chi-Fe5C2. *Powder Diffr.* **1999**, *14*, 130−132.

(26) Jiang, F.; Liu, B.; Li, W. P.; Zhang, M.; Li, Z. J.; Liu, X. H. Two-dimensional graphene-directed formation of cylindrical iron carbide nanocapsules for Fischer−Tropsch synthesis. *Catal. Sci. Technol.* **2017**, *7*, 4609−4621.

(27) Yin, J.; Liu, X.; Liu, X.-W.; Wang, H.; Wan, H.; Wang, S.; Zhang, W.; Zhou, X.; Teng, B.-T.; Yang, Y.; Li, Y.-W.; Cao, Z.; Wen, X.-D. Theoretical exploration of intrinsic facet-dependent CH4 and C2 formation on Fe5C2 particle. *Appl. Catal., B* **2020**, *278*, 119308.

(28) Pham, T. H.; Qi, Y. Y.; Yang, J.; Duan, X. Z.; Qian, G.; Zhou, X. G.; Chen, D.; Yuan, W. K. Insights into Flagg Iron-Carbide-Catalyzed Fischer−Tropsch Synthesis: Suppression of CH4 Formation and Enhancement of C-C Coupling on chi-Fe5C2 (510). *ACS Catal.* **2015**, *5*, 2203−2208.

(29) Zhang, M.; Ren, J.; Yu, Y. Insights into the Hydrogen Coverage Effect and the Mechanism of Fischer−Tropsch to Olefins Process on Fe5C2 (510). *ACS Catal.* **2020**, *10*, 689−701.

(30) Li, T.; Wen, X.; Yang, Y.; Li, Y.-W.; Jiao, H. Mechanistic Aspects of CO Activation and C−C Bond Formation on the Fe/C- and Fe-Terminated Fe3C(010) Surfaces. *ACS Catal.* **2020**, *10*, 877−890.

(31) Ozbek, M. O.; Niemantsverdriet, J. W. Elementary reactions of CO and H 2 on C-terminated ε-Fe 5 C 2 (0 0 1) surfaces. *J. Catal.* **2014**, *317*, 158−166.

(32) He, Y.; Zhao, P.; Yin, J.; Guo, W.; Yang, Y.; Li, Y.-W.; Huo, C.-F.; Wen, X.-D. CO Direct versus H-Assisted Dissociation on Hydrogen Coadsorbed ε-Fe5C2 Fischer−Tropsch Catalysts. *J. Phys. Chem. C* **2018**, *122*, 20907−20917.

(33) Cheng, J.; Hu, P.; Ellis, P.; French, S.; Kelly, G.; Lok, C. M. Density Functional Theory Study of Iron and Cobalt Carbides for Fischer−Tropsch Synthesis. *J. Phys. Chem. C* **2010**, *114*, 1085−1093.

(34) Gracia, J. M.; Prinsloo, F. F.; Niemantsverdriet, J. W. Mars-van Krevelen-like Mechanism of CO Hydrogenation on an Iron Carbide Surface. *Catal. Lett.* **2009**, *133*, 257−261.

(35) Dry, M. E. The Fischer−Tropsch process: 1950−2000. *Catal. Today* **2002**, *71*, 227−241.

(36) Xie, J.; Yang, J.; Dugulan, A. I.; Holmen, A.; Chen, D.; de Jong, K. P.; Louwerse, M. J. Size and Promoter Effects in Supported Iron Fischer−Tropsch Catalysts: Insights from Experiment and Theory. *ACS Catal.* **2016**, *6*, 3147−3157.

(37) Huang, S. D.; Shang, C.; Zhang, X. J.; Liu, Z. P. Material discovery by combining stochastic surface walking global optimization with a neural network. *Chem. Sci.* **2017**, *8*, 6327−6337.

(38) Huang, S. D.; Shang, C.; Kang, P. L.; Liu, Z. P. Atomic structure of boron resolved using machine learning and global sampling. *Chem. Sci.* **2018**, *9*, 8644−8655.

(39) Huang, S. D.; Shang, C.; Kang, P. L.; Zhang, X. J.; Liu, Z. P. LASP: Fast global potential energy surface exploration. *Wiley Interdiscip. Rev.: Comput. Mol. Sci.* **2019**, *9*, No. e1415.

(40) Shang, C.; Liu, Z. P. Stochastic Surface Walking Method for Structure Prediction and Pathway Searching. *J. Chem. Theory Comput.* **2013**, *9*, 1838−1845.

(41) Shang, C.; Zhang, X. J.; Liu, Z. P. Stochastic surface walking method for crystal structure and phase transition pathway prediction. *Phys. Chem. Chem. Phys.* **2014**, *16*, 17845−17856.

(42) Shang, C.; Zhao, W. N.; Liu, Z. P. Searching for new TiO2 crystal phases with better photoactivity. *J. Phys.: Condens. Matter* **2015**, *27*, 134203.

(43) Zhang, X. J.; Shang, C.; Liu, Z. P. Stochastic surface walking reaction sampling for resolving heterogeneous catalytic reaction network: A revisit to the mechanism of water-gas shift reaction on Cu. *J. Chem. Phys.* **2017**, *147*, 152706.

(44) Behler, J.; Parrinello, M. Generalized neural-network representation of high-dimensional potential-energy surfaces. *Phys. Rev. Lett.* **2007**, *98*, 146401.



https://doi.org/10.1021/jacs.1c04624
J. Am. Chem. Soc. 2021, 143, 11109−11120

(45) Behler, J. Representing potential energy surfaces by high-dimensional neural network potentials. *J. Phys.: Condens. Matter* **2014**, *26*, 183001.
(46) Shang, C.; Liu, Z.-P. LASP G-NN Datasets, http://www.lasphub.com/supportings/Trainfile_FeCHO.tar.gz (accessed2021−0708), *FeCHO dataset download*.
(47) Kresse, G.; Furthmuller, J. Efficient iterative schemes for ab initio total-energy calculations using a plane-wave basis set. *Phys. Rev. B: Condens. Matter Mater. Phys.* **1996**, *54*, 11169−11186.
(48) Perdew, J. P.; Burke, K.; Ernzerhof, M. Generalized gradient approximation made simple. *Phys. Rev. Lett.* **1996**, *77*, 3865−3868.
(49) Zhang, X.-J.; Shang, C.; Liu, Z.-P. Double-Ended Surface Walking Method for Pathway Building and Transition State Location of Complex Reactions. *J. Chem. Theory Comput.* **2013**, *9*, 5745−5753.
(50) Zhang, X.-J.; Liu, Z.-P. Variable-Cell Double-Ended Surface Walking Method for Fast Transition State Location of Solid Phase Transitions. *J. Chem. Theory Comput.* **2015**, *11*, 4885−4894.
(51) Shang, C.; Liu, Z.-P. Constrained Broyden Minimization Combined with the Dimer Method for Locating Transition State of Complex Reactions. *J. Chem. Theory Comput.* **2010**, *6*, 1136−1144.
(52) Shang, C.; Liu, Z.-P. Constrained Broyden Dimer Method with Bias Potential for Exploring Potential Energy Surface of Multistep Reaction Process. *J. Chem. Theory Comput.* **2012**, *8*, 2215−2222.
(53) Guan, S. H.; Zhang, X. J.; Liu, Z. P. Energy Landscape of Zirconia Phase Transitions. *J. Am. Chem. Soc.* **2015**, *137*, 8010−8013.
(54) Chen, X. Q.; Deng, D. H.; Pan, X. L.; Hu, Y. F.; Bao, X. H. N-doped graphene as an electron donor of iron catalysts for CO hydrogenation to light olefins. *Chem. Commun.* **2015**, *51*, 217−220.
(55) Yuan, X. Z.; Zhou, Y. W.; Huo, C. F.; Guo, W. P.; Yang, Y.; Li, Y. W.; Wen, X. D. Crystal Structure Prediction Approach to Explore the Iron Carbide Phases: Novel Crystal Structures and Unexpected Magnetic Properties. *J. Phys. Chem. C* **2020**, *124*, 17244−17254.
(56) Eckstrom, H. C.; Adcock, W. A. A New Iron Carbide in Hydrocarbon Synthesis Catalysts. *J. Am. Chem. Soc.* **1950**, *72*, 1042−1043.
(57) Herbstein, F. H.; Snyman, J. A. Identification of Eckstrom-Adcock Iron Carbide as Fe7c3. *Inorg. Chem.* **1964**, *3*, 894−896.
(58) Fruchart, R.; Rouault, A. Twin Crystals of Orthorhombic Isomorphous Cr7c3, Mn7c3, Fe7c3 Carbides. *Ann. Chim. France* **1969**, *4*, 143.
(59) Audier, M.; Bowen, P.; Jones, W. Transmission Electron-Microscopic Study of Single-Crystals of Fe7c3. *J. Cryst. Growth* **1983**, *63*, 125−134.
(60) Zhang, X. J.; Shang, C.; Liu, Z. P. Pressure-induced silica quartz amorphization studied by iterative stochastic surface walking reaction sampling. *Phys. Chem. Chem. Phys.* **2017**, *19*, 4725−4733.
(61) Chen, S.; Ma, S.; Liu, Z.-P. Zirconia-Supported ZnO Single Layer for Syngas Conversion Revealed from Machine-Learning Atomic Simulation. *J. Phys. Chem. Lett.* **2021**, *12*, 3328−3334.
(62) Li, X.-T.; Chen, L.; Shang, C.; Liu, Z.-P. In Situ Surface Structures of PdAg Catalyst and Their Influence on Acetylene Semihydrogenation Revealed by Machine Learning and Experiment. *J. Am. Chem. Soc.* **2021**, *143*, 6281−6292.
(63) Chen, B. X.; Wang, D.; Duan, X. Z.; Liu, W.; Li, Y. F.; Qian, G.; Yuan, W. K.; Holmen, A.; Zhou, X. G.; Chen, D. Charge-Tuned CO Activation over a chi-Fe5C2 Fischer−Tropsch Catalyst. *ACS Catal.* **2018**, *8*, 2709−2714.
(64) Huo, C. F.; Li, Y. W.; Wang, J. G.; Jiao, H. J. Insight into CH4 Formation in Iron-Catalyzed Fischer−Tropsch Synthesis. *J. Am. Chem. Soc.* **2009**, *131*, 14713−14721.
(65) Liu, B.; Li, W. P.; Zheng, J.; Lin, Q.; Zhang, X.; Zhang, J. W.; Jiang, F.; Xu, Y. B.; Liu, X. H. CO2 formation mechanism in Fischer−Tropsch synthesis over iron-based catalysts: a combined experimental and theoretical study. *Catal. Sci. Technol.* **2018**, *8*, 5288−5301.
(66) van Steen, E.; Schulz, H. Polymerisation kinetics of the Fischer−Tropsch CO hydrogenation using iron and cobalt based catalysts. *Appl. Catal., A* **1999**, *186*, 309−320.
(67) Sarkari, M.; Fazlollahi, F.; Ajamein, H.; Atashi, H.; Hecker, W. C.; Baxter, L. L. Catalytic performance of an iron-based catalyst in Fischer−Tropsch synthesis. *Fuel Process. Technol.* **2014**, *127*, 163−170.
(68) Van der Laan, G. P.; Beenackers, A. A. C. M. Kinetics and selectivity of the Fischer−Tropsch synthesis: A literature review. *Catal. Rev.: Sci. Eng.* **1999**, *41*, 255−318.


https://doi.org/10.1021/jacs.1c04624
*J. Am. Chem. Soc.* 2021, 143, 11109−11120